On the accurate prediction of turbine power and thrust using BEM and CFD

Yabin Liu, Stefano Gambuzza, Riccardo Broglia, Anna M. Young, Edward D. McCarthy, and Ignazio Maria Viola

***Abstract*—We compute the loads on a model-scale tidal turbine with Blade Element Momentum (BEM) theory and Computational Fluid Dynamics (CFD) simulations, and we compare the results with towing tank tests. CFD simulations are wall-resolved, steady, Reynolds-averaged Navier-Stokes simulations with a $k-\omega$ SST turbulence model, where only a 120° wedge domain with a single blade is resolved in a non-inertial frame of reference. We undertake a detailed uncertainty analysis to identify the sources of error. BEM uncertainty is computed with a Monte-Carlo approach based on the differences in the predictions of CFD and Xfoil for the sectional lift and drag coefficients,while CFD uncertainty is based on the errors due to the finite number of iterations and spatial resolution.**

The maximum error of CFD (8.0%) with respect to the experimental data is about half of that of BEM (15.5%) for the power (C_P) and the thrust (C_T) coefficients and both errors are within 4.1% for CFD and within 7.2% for BEM around the optimal tip-speed ratio ($\lambda = 6.03$). The BEM error is within the uncertainty associated with the imprecise knowledge of the sectional lift and drag coefficients. The sectional forces from CFD and BEM disagree at both the tip and the root, resulting in a substantial BEM underprediction of C_P at high λ values (up to 15.5%), yet C_T is well predicted (within 2.3%) at every λ. The CFD uncertainty is markedly smaller than the error, which is thus mostly due to a modelling error such as the turbulence model, the neglected effect of the support structure, the free surface, and the imprecise knowledge of the input conditions. Overall these results suggest that CFD provides both a maximum error and uncertainty that are substantially smaller than that of BEM, but both methods suffer from modelling errors that require further investigation.

***Index Terms*—Tidal energy, tidal turbine hydrodynamics, computational fluid dynamics, blade-resolved Reynolds-averaged Navier-Stokes simulations, blade element momentum theory.**

I. Introduction

HARVESTING energy from tidal current can contribute to the transition to sustainable use of renewable energy. Tidal power can provide 34 TWh/year in the UK alone [1]. The performance of tidal turbines, as the key energy conversion component in tidal power systems, plays a crucial role in effectively exploiting tidal energy. Accurately predicting the energy-harvesting efficiency of turbines and the associated flow physics is essential to assess and improve the turbine performance through optimised hydrodynamic design [2]. To improve confidence in modelling techniques and establish good practice, the UK Supergen Offshore Renewable Energy Hub has run an Unsteady Loading Tidal Turbine Benchmarking Study [3]. Experiments were performed in a towing tank at a Reynolds number of 1.3×10^6 based on the constant towing velocity $U_\infty = 1$ m s^{-1} and the turbine diameter $D = 1.6$ m. The tested geometry, as well as the flow and operating conditions, were made available to different groups to make a blind prediction of the measured forces and power [4]. This paper presents the details of the BEM simulations and the CFD simulations performed at the University of Edinburgh, for which a detailed analysis of the numerical uncertainties has been undertaken.

This work was supported by the UK Engineering and Physical Sciences Research Council through the grant 'Morphing-Blades: New-Concept Turbine Blades for Unsteady Load Mitigation' [EP/V009443/1]

YL, SG, EMcC, and IMV are with the School of Engineering, University of Edinburgh, Edinburgh EH9 3BF, UK (e-mail for correspondence: I.M.Viola@ed.ac.uk).

AY is with the Department of Mechanical Engineering, University of Bath, Bath, BA2 7AY, UK.

RB is with the Institute for Marine Engineering, National Research Council, Rome 00128, Italy.

Digital Object Identifier:
https://doi.org/10.36688/ewtec-2023-505

II. Blade element momentum theory

BEM simulations are performed with `transTide` [5], [6], a BEM solver developed in-house that predicts the loads generated by a tidal turbine subject to turbulent, sheared, and yawed inflow conditions ~~in the presence of yaw~~. Each of these features can be toggled individually, and the simulations reported here do not make use of any of these features. A detailed rundown of the practical implementation of turbulence in this code is reported in detail in Scarlett et al. [5] and Scarlett and Viola [6], and the code has been used and validated for tidal-energy applications by Pisetta et al [7]–[10].

The sectional lift (C_L) and drag (C_D) coefficients are computed with XFOIL [11] and are a function of the local angle of attack α and the local Reynolds number Re_c. The chord-based Reynolds number is assumed only a function of the radial coordinate r and not of the tip-speed ratio λ, i.e.

$$Re_c = \frac{U_\infty c(r)}{\nu}\sqrt{1+\left(\frac{r\lambda_\mathrm{D}}{R}\right)^2}, \tag{1}$$

where $c(r)$ is the local chord as function of the radial coordinate r; ν is the dynamic viscosity of water; $R = D/2$ is the rotor diameter, and $\lambda_D = 6.03$ is the design tip-speed ratio. We specify the critical amplification number N_cr [12] as a constant value of nine over the

whole blade. Results are averaged over five rotational periods.

We assume that the main source of error is in the estimate of the sectional lift and drag coefficients. This is estimated through the difference between the values of the coefficients computed with Xfoil (C_L^{XFOIL} and C_D^{XFOIL}) and those computed with CFD by the benchmark organisers (C_L^{RANS} and C_D^{RANS}). We compute the 95% confidence interval in the estimate of the coefficients by multiplying the error by a factor of safety of three [13],

$$E_{C_L} = 3 \max_{\alpha} \left(|C_L^{\text{RANS}} - C_L^{\text{XFOIL}}| \right) , \tag{2}$$

$$E_{C_D} = 3 \max_{\alpha} \left(|C_D^{\text{RANS}} - C_D^{\text{XFOIL}}| \right) . \tag{3}$$

The uncertainty in the BEM results is estimated with a Monte-Carlo approach as follows. For each test case, the simulations are run 500 times, changing the lift coefficients for each section by a constant, random value δ_L and the drag by a constant, random δ_D; these are drawn from normal distributions having zero mean and standard deviations respectively $E_{C_L}/2$ and $E_{C_D}/2$. Then, for every generic quantity x via BEM, we compute the width of the $95\,\%$ confidence interval as

$$E_x = \frac{2\,\sigma_x}{\sqrt{N}} , \tag{4}$$

where σ_x is the standard deviation of $N = 500$ independent estimations of x.

III. Computational fluid dynamics

A. Numerical methods

We solve the steady-state Reynolds-averaged Navier-Stokes (RANS) equations with the open-source tool OpenFOAMv2106. We employ the `simpleFoam` solver with the SST $k-\omega$ turbulence model. We model a third of the turbine rotor (Figure 1), and we solve the governing equations for a non-inertial rotating frame of reference. The computational domain is a 120° slice of a cylinder, whose axis coincides with that of the tested turbine. The domain is $17D$ in length along the streamwise direction and has a radius of $2.5D$. We set uniform, constant free stream velocity with zero turbulence at the upstream inlet boundary; constant zero pressure at the downstream outlet boundary; slip condition at the outer side boundary; periodic condition at the two inner side boundaries; and no-slip condition at the blade and hub surface. The domain is discretised using ICEM-CFD with a non-conformal structural mesh of 19M hexahedral cells (Figure 2). The blade's boundary layer is resolved with y^+ below 0.3 at the design tip-speed ratio $\lambda = 6.03$ (Figure 3). The growth ratio of the grid size inside the blade boundary layer is about 1.1.

The rotational `cyclicAMI` interface tool is employed to couple the periodic domains. A Semi-Implicit Method for Pressure Linked Equations-Consistent algorithm is used for the pressure-velocity coupling, while the Gauss linear scheme is used for gradients and the bounded Gauss upwind scheme for the divergence. The pressure solver is set as a Generalised Geometric-Algebraic Multi-Grid, and the smoother solver Gauss-Seidel is employed for the other terms.

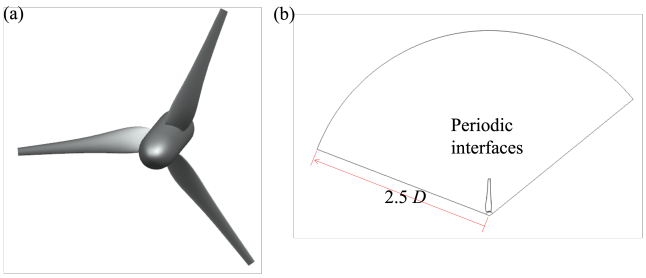

Fig. 1. Complete geometry of the modelled turbine, (a) and axial view of the 120°-wedge computational domain (b).

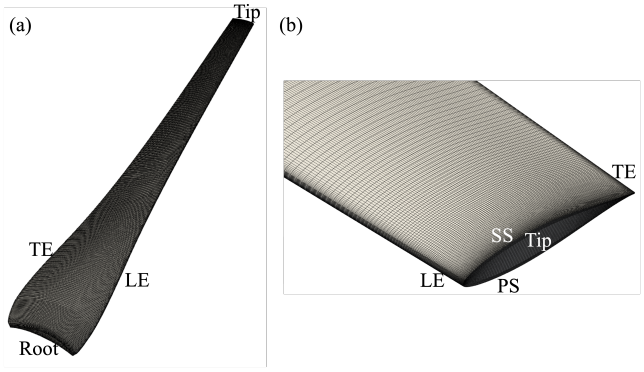

Fig. 2. Mesh on the blade surface (a) and detailed view near the tip (b). LE: leading edge; TE: trailing edge; PS: pressure side; SS: suction side.

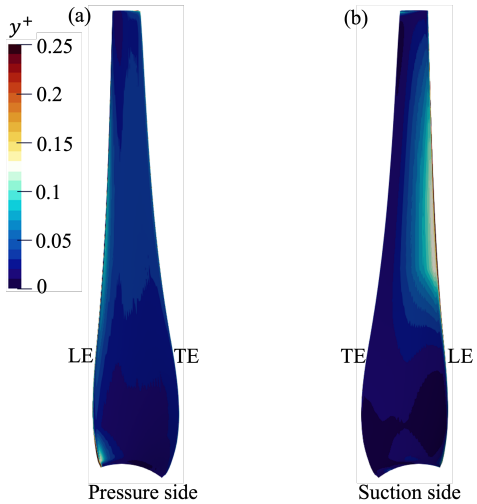

Fig. 3. y^+ distribution on the pressure (a) and suction (b) side of the blade surface at $\lambda = 6.03$.

B. Verification - Uncertainty quantification

The uncertainty of the CFD simulation is computed following the least square approach proposed by Viola et al. [14] that is summarised hereby. This method was originally developed for yacht sails. It was successively adopted for a wide range of applications, including the flow past the pappus of the dandelion diaspore

[15], permeable disks [16], oscillating flapping foils [17], vertical-axis [18] and horizontal-axis turbines [19], arrays of energy harvesters [20], and ship hulls [21].

The verification process is set out to estimate the absolute (E_Φ) or the relative uncertainty (U_Φ) at 95% confidence level in the estimate of the quantity Φ, which here is either the power or the thrust coefficient, where

$$E_\Phi = \Phi U_\Phi. \tag{5}$$

The relative numerical uncertainty is estimated independently for each source of error, including that due to the finite grid resolution (U_{Φ_g}), the finite time step (U_{Φ_t}), the round-off (U_{Φ_r}), and the finite number of iterations (U_{Φ_c}). In this work, U_{Φ_t} is not assessed because the simulations are steady, and U_{Φ_r} is considered negligible because double precision is used. The uncertainty due to the finite spatial resolution is estimated by undertaking simulations with different grid resolutions. The same procedure could be followed to compute U_{Φ_t} if the simulations were unsteady, testing different time resolutions. Take h as the relative step size of the resolution, i.e. the ratio between the linear grid size of the current and the reference grid. We define

$$\varphi(h) \equiv \frac{\Phi(h)}{\Phi(\text{base})}, \tag{6}$$

where $\Phi(\text{base})$ is the value of the computed solution with the base grid size for which the uncertainty is computed. We fit $\varphi(h)$ with

$$\varphi(h) \approx \zeta h^\xi + \varphi_0. \tag{7}$$

The coefficients ζ, ξ and φ_0 are exactly determined when $\varphi(h)$ is known for only three values of h; otherwise, they are computed with a least-squares method and σ is the standard deviation of the fit.

The relative numerical uncertainty due to the spatial resolution (i.e. with $U_{\Phi_g} = U_{\Phi_h}$) is

$$U_{\Phi_h} = \begin{cases} 1.25 \mid 1 - \varphi_0 \mid + \sigma & p \geq 0.95, \\ 1.5 \frac{\varphi_{\max} - \varphi_{\min}}{1 - \frac{h_{\min}}{h_{\max}}} + \sigma & p < 0.95. \end{cases} \tag{8}$$

where $\varphi_{\max}$ and $\varphi_{\min}$ are the maximum and the minimum of $\varphi(h)$, whilst $h_{\max}$ and $h_{\min}$ are the maximum and the minimum of h. Here the grid uncertainty is computed through a set of simulations with three geometrically similar grids with a number of cells ranging from 7.3×10^6 to 1.94×10^7.

The convergence error is computed by fitting the computed solution over 10 000 iterations, after having discarded the first 2000 iterations, with a function that tends asymptotically to a constant value. The error is the difference between the asymptotic value and the solution of the last iteration. The uncertainty is the product of the error and a factor of safety of 1.25. Finally, the uncertainty is increased by the standard deviation of the fit.

The total relative numerical uncertainty is

$$U_\Phi = \sqrt{U_{\Phi_g}^2 + U_{\Phi_t}^2 + U_{\Phi_r}^2} + U_{\Phi_c}, \tag{9}$$

where $U_{\Phi_t} = U_{\Phi_r} = 0$ in this work. It is noted that U_{Φ_c} is not under the square root because it is not considered independent from the other sources of error.

IV. Results

A. Flow field

The constrained streamlines on the blade surface are presented in Figures 4 and 5 at three tip-speed ratios, based on the CFD results. Flow separation is observed at $\lambda = 4.52$ on the blade suction surface. When the tip-speed ratio increases to $\lambda = 6.03$ and $\lambda = 7.54$, flow separation is only observed at the blade tip and the blade root. The region of flow separation near the blade root shrinks with increasing tip-speed ratios, while flow separation persists even at high λ values near the tip, as shown in Figure 5. The 3D vortex structures around the blade are present in Figure 6, which shows the $-2 \times 10^4 U_\infty^2 / D^2$ isosurface.

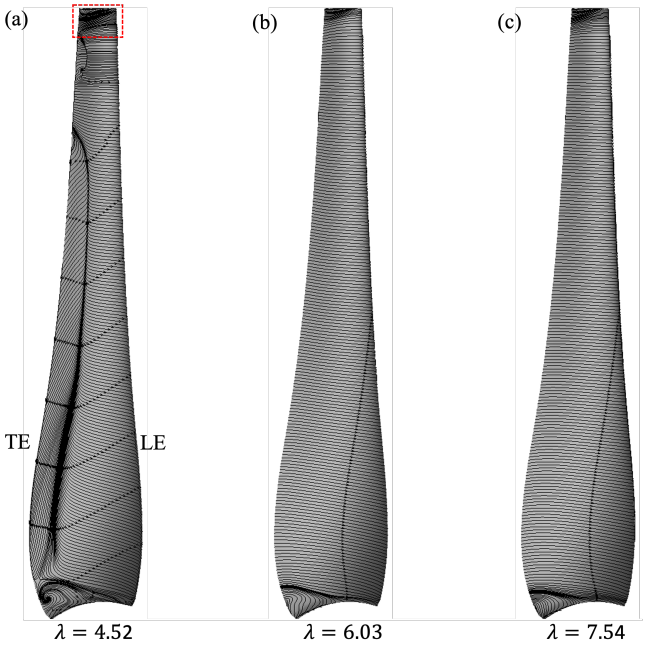

Fig. 4. Constrained streamlines on the blade suction surface at tip-speed ratios 4.52 (a), 6.03 (b) and 7.54 (c).

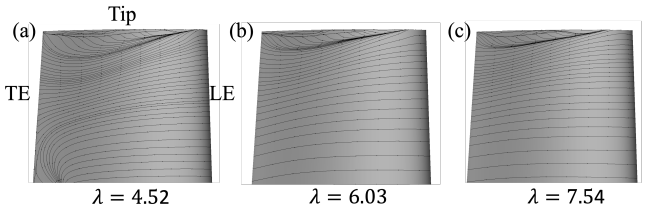

Fig. 5. Constrained streamlines on the blade surface near the blade tip (i.e. in the region inside of the red dashed rectangle in Figure 4) at tip-speed ratios 4.52 (a), 6.03 (b) and 7.54 (c).

B. Uncertainty in the estimate of C_P and C_T

Simulations were carried out for a range of tip-speed ratios from 4.52 to 7.54. The overall numerical uncertainty for C_P and C_T for both BEM and CFD

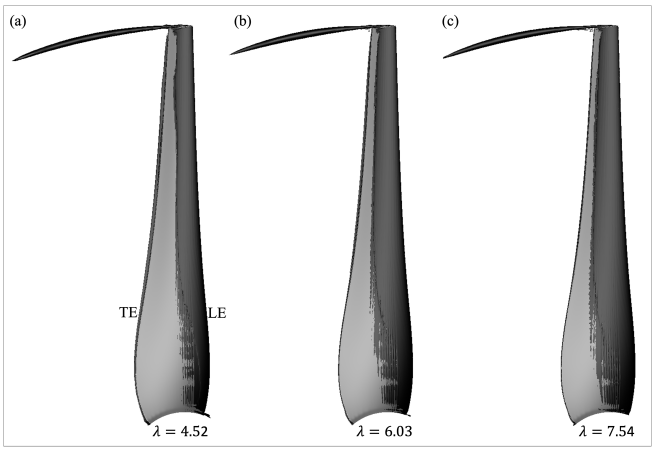

Fig. 6. Vortex structures around the blade, visualised by isosurface of lambda-2 criterion, at tip-speed ratios 4.52 (a), 6.03 (b) and 7.54 (c).

is shown in Figure 7. The BEM uncertainty is up to 6.0% for C_P and 2.6% for C_T, while CFD uncertainty is always within 3.9% for both C_T and C_P. Interestingly, the uncertainty on C_P is much greater than that on C_T at high tip speed ratios for both BEM and CFD, a consequence of the larger uncertainty on the sectional drag value than on the sectional lift value. It is noted that the CFD uncertainty is broken down as follows. The convergence uncertainty U_{Φ_c} is between 0.05% and 0.96% for C_P, and between 0.06% to 0.4% for C_T. The grid uncertainty U_{Φ_g} is between 0.33% to 3.89% for C_P, and between 0.02% and 3.59% for C_T.

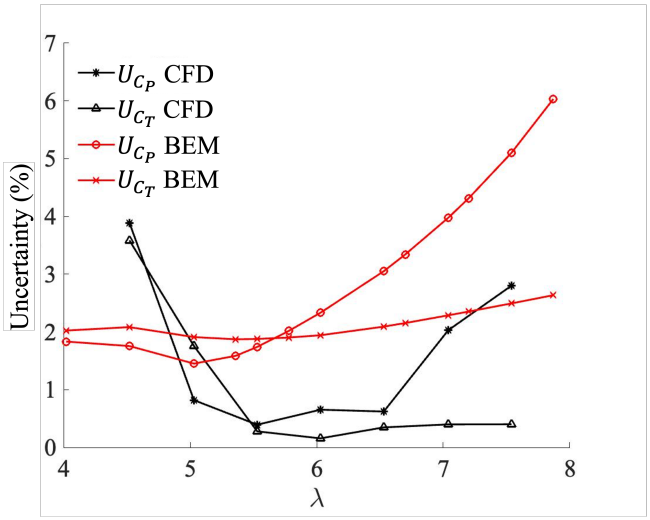

Fig. 7. Uncertainty in the estimate of C_P and C_T with CFD and BEM for various tip-speed ratios.

C. Power and thrust coefficients

Figure 8 shows C_P computed with BEM, CFD and the experimental data [3]. BEM underpredicts the power coefficient with respect to the experiment, and the error increases with increasing λ up to 15.5% at $\lambda = 7.87$. The BEM uncertainty, which is shown by error bars in Figure 8, is much smaller than the error, suggesting that some critical physics are incorrectly modelled and that the role of these physics increases with λ. This is potentially associated with the high-induction correction, which is here implemented using the Buhl correction [6].

In contrast, the relative error of the CFD prediction decreases with increasing λ: from 8.0% at $\lambda = 4.52$ to 1.8% at $\lambda = 6.53$. The error is of the same order of magnitude as the CFD uncertainty, suggesting that any modelling error is small or absent relative to the numerical error.

Figure 9 shows C_T computed with BEM and CFD. The BEM prediction of C_T is in better agreement with the experiments than the CFD prediction. The error is lower than 2.1% at every λ. The uncertainty is higher than the error, suggesting that the error could be due to the incorrect estimate of the sectional lift and drag, and thus it is not possible to identify any error due to incorrectly modelled or neglected physics. The error in the CFD simulations is 2.3% at $\lambda = 5.53$ and 1.8% at $\lambda = 6.53$ near where C_P is maximum, while it is higher both at low and high tip speed ratios. Note that this trend is consistent with that of the uncertainty. At low tip-speed ratios, the error is up to 7.9% at $\lambda = 4.52$, and it might be attributed to underpredicted flow separation.

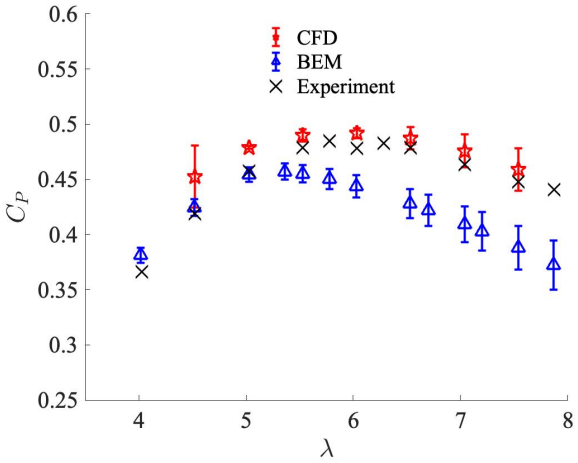

Fig. 8. Power coefficient versus the tip-speed ratio computed with BEM, CFD and comparison with experimental data [3].

D. Sectional force coefficients

We now focus on the difference between the sectional force coefficients selected by the BEM code and those computed with CFD. The lift and drag directions depend on the local angle of attack, which is computed by the BEM for each blade section but is not uniquely defined in the CFD simulations. Hence, we instead consider the edgewise and flapwise force components, i.e. the force components parallel and orthogonal to the rotor plane, respectively. For each of these, we define the force coefficient C_F (edgewise or flapwise) as

$$C_F(r) \equiv \frac{F(r)}{\frac{1}{2}\rho U_\infty^2 \pi R}, \tag{10}$$

where $F(r)$ is the sectional force component (edgewise or flapwise) at the blade spanwise location r.

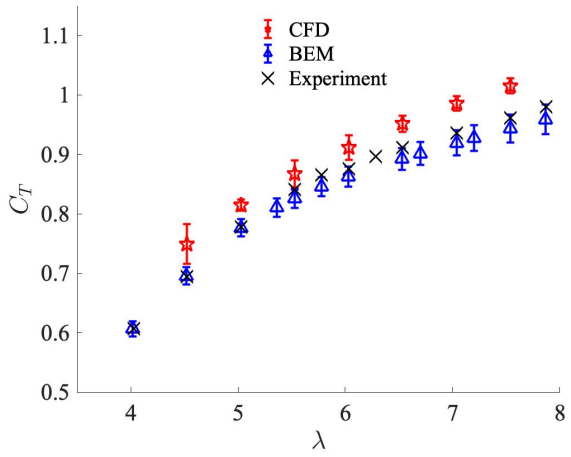

Fig. 9. Thrust coefficient versus the tip-speed ratio computed with BEM, CFD and comparison with experimental data [3].

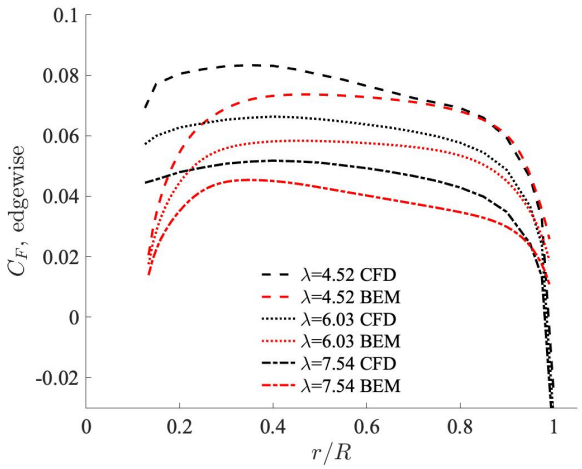

Fig. 10. Edgewise force distribution along the blade span for three tip-speed ratios computed with BEM, CFD.

Figure 10 shows the spanwise distribution of the edgewise force coefficient $C_{F,\text{edgewise}}$ at three tip-speed ratios. The maximum value of $C_{F,\text{edgewise}}$ is nearer the root at low λ and nearer the tip at high λ. For all values of λ shown, the prediction from CFD is higher than that of the BEM over the inboard part of the span, and the difference increases with decreasing distance from the root. This discrepancy suggests an excessive root correction of the force coefficients at the root in the BEM code, and could be due to the turbine design: the sections blade sections remain streamlined up to the hub intersection instead of becoming cylindrical near the root as in most common designs (see Figure 4). However, CFD predicts higher values not only close to the root but for most of the blade span. This difference in spanwise force coefficients is consistent with the better match of the experimental power curve by the CFD than BEM (Figure 8), as the power is given by the integral of the edgewise force along the span multiplied by the angular velocity.

Figure 11 shows the spanwise distribution of the flapwise force coefficient $C_{F,\text{flapwise}}$ at three tip-speed ratios. The maximum value of $C_{F,\text{flapwise}}$ is reached at around $r = 85\%R$ for each tip-speed ratio, and $C_{F,\text{flapwise}}$ increases with λ. The force peaks predicted by BEM are higher and closer to the tip than those predicted with CFD, while the force is lower near the root than that predicted with CFD.

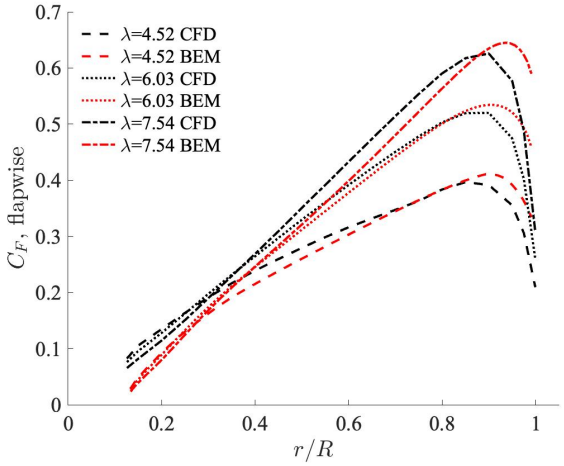

Fig. 11. Flapwise force distribution along the blade span for three tip-speed ratios computed with BEM, CFD.

E. Bending moment

Experimental data is not available for the flapwise and edgewise force distributions along the span. Instead, the bending moment M_B was measured at 5 locations along the span. The edgewise and flapwise bending moment at the radial coordinate r' is computed with BEM and CFD as the integral of the first moment of the edgewise and flapwise force,

$$M_B(r') \equiv \int_{r'}^{R} (r - r')F(r)\mathrm{d}r. \tag{11}$$

We define the bending moment coefficient as

$$C_{BM}(r) \equiv \frac{M_B(r)}{\frac{1}{16}\rho U_\infty^2 \pi D^3}. \tag{12}$$

It must be noted that the bending moment vanishes at the tip by definition. Differences between BEM, CFD and experiments would inevitably increase towards the root. However, the main contributor to the differences between these curves near the root is mostly due to differences in the forces nearer the tip rather than the root, due to the weighting function r in equation 11.

Figures 12 to 14 show the edgewise bending moment coefficient along the blade span for the BEM and CFD cases for three λ values. The CFD prediction is in greater agreement with the experiments than the BEM prediction at tip-speed ratios, except for $\lambda = 4.52$. The discrepancy between the BEM and experiment results increases at higher tip-speed ratios. These results are consistent with the prediction of C_P shown in Figure 8.

The distribution of the flapwise bending moment coefficient along the blade span computed with BEM, CFD, and experimentally is shown in Figures 15 to 17 for $\lambda = 4.52$, 6.03 and 7.54, respectively. The difference

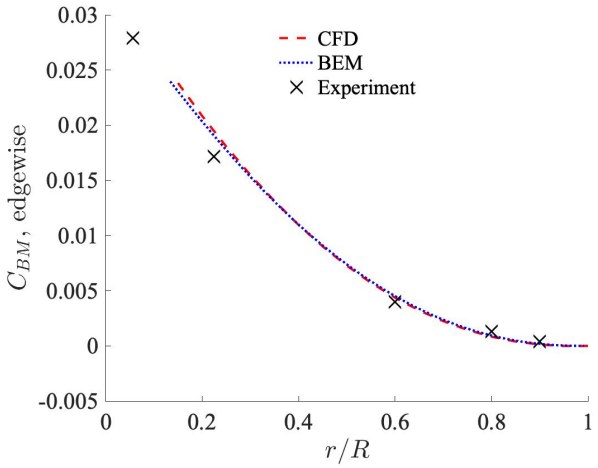

Fig. 12. Edgewise bending moment distribution along the blade span at $\lambda = 4.52$ computed with BEM, CFD and comparison with experimental data [3].

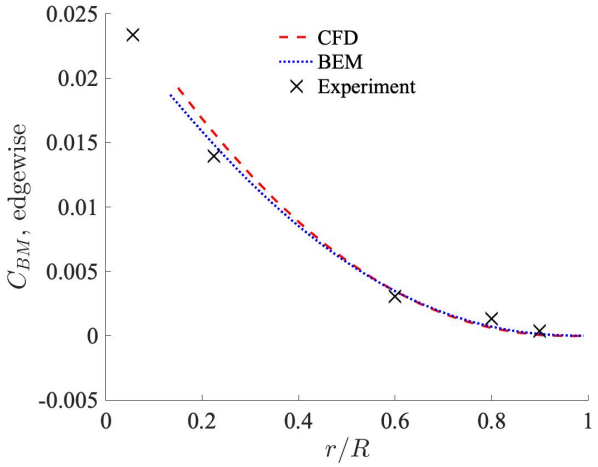

Fig. 13. Edgewise bending moment distribution along the blade span at $\lambda = 6.03$ computed with BEM, CFD and comparison with experimental data [3]..

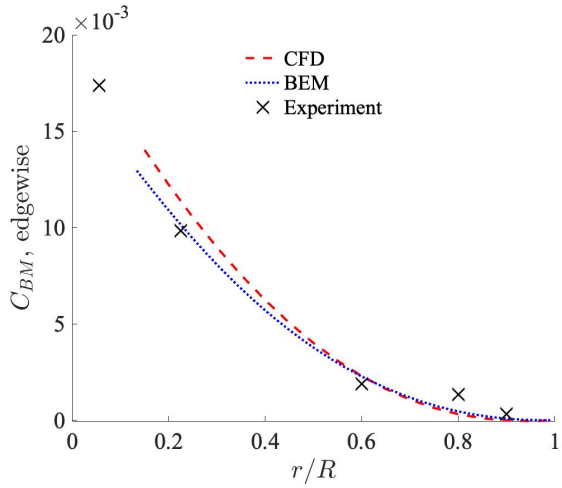

Fig. 14. Edgewise bending moment distribution along the blade span at $\lambda = 7.54$ computed with BEM, CFD and comparison with experimental data [3].

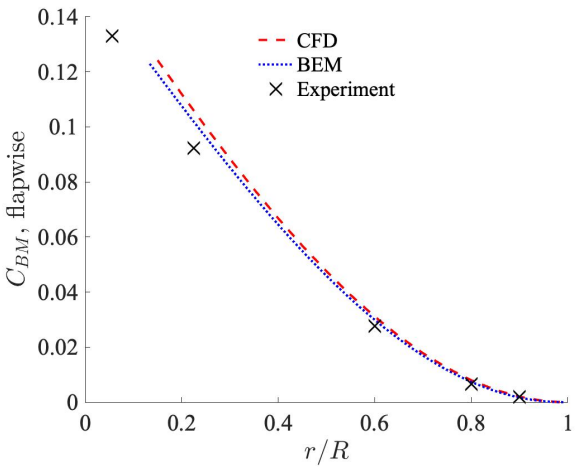

Fig. 15. Flapwise bending moment distribution along the blade span at $\lambda = 4.52$ computed with BEM, CFD and comparison with experimental data [3].

between the values predicted with CFD and BEM is relatively small compared to the difference with the experimental values, which are generally lower than those predicted. However, the BEM results are in closer agreement with the experiments, which is consistent with the better agreement in C_T shown in Figure 9.

V. Conclusion

In this paper, we computed the loads on a model-scale tidal turbine based on BEM theory and CFD, and we compared the results with towing tank tests. We estimated the uncertainty of the BEM results with a Monte-Carlo approach based on the difference between the CFD and Xfoil values of the sectional lift and drag coefficients, and the uncertainty is below 6.0% for C_P and 2.6% for C_T. The CFD uncertainty is made of the grid uncertainty and the convergence uncertainty, which are below 3.89% and 0.96%, respectively, for both power and thrust for λ from 4.52 to 7.54.

BEM tends to underpredict the thrust by less than 2.3% at any λ value, while the power is increasingly underpredicted with increasing λ up to 15.5% at $\lambda = 7.87$. Remarkably, BEM provides an excellent power and thrust prediction at low λ, where CFD predicts a marked trailing edge separation. In contrast, CFD tends to overpredict the power and the thrust by no more than 4.1% around the optimal tip-speed ratio ($\lambda = 6.03$), while the error increases up to 8.0% at both low and high λ values. The maximum error of CFD (8.0%) is about half of that of BEM (15.5%), but both show give smaller errors at the optimal λ.

The uncertainty analysis shows that the differences between the experimental data and the BEM prediction are within the uncertainty associated with the imprecise knowledge of the sectional lift and drag coefficients. The CFD and BEM sectional forces at the tip and root are substantially different. Still, no conclusions can be made on the accuracy of the high induction and edge corrections in the BEM because of the good prediction of the thrust (within 2.3%). The CFD numerical uncertainty due to the finite spatial resolution and number of iterations is markedly smaller than the maximum numerical-experimental error at low and high λ values, and it is thus mostly due to

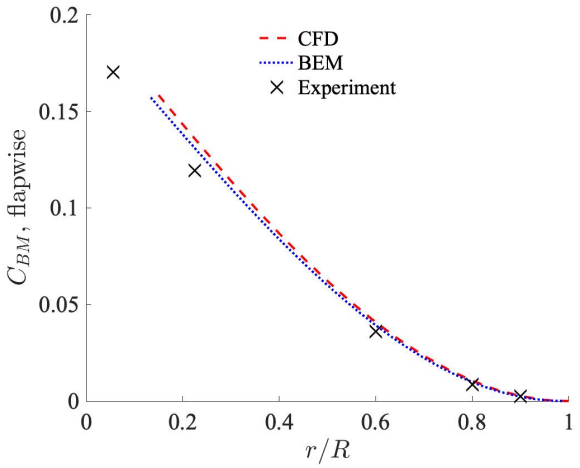

Fig. 16. Flapwise bending moment distribution along the blade span at $\lambda = 6.03$ computed with BEM, CFD and comparison with experimental data [3].

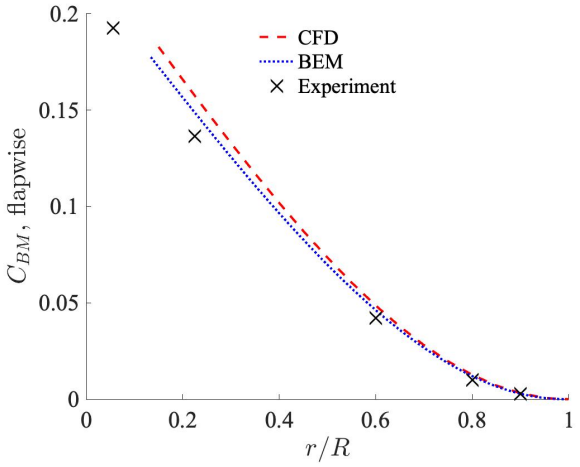

Fig. 17. Flapwise bending moment distribution along the blade span at $\lambda = 7.54$ computed with BEM, CFD and comparison with experimental data [3].

modelling errors such as the turbulence model, the neglected support structure and free surface, and the imprecise knowledge of the input values. Interestingly, the uncertainty is relatively higher at low and high λ values, where the error is also higher.

Overall these results suggest that CFD allows both a maximum error and uncertainty that are substantially smaller than that of BEM, but both methods suffer from modelling errors that require further investigation.

REFERENCES

[1] D. Coles, A. Angeloudis, D. Greaves, G. Hastie, M. Lewis, L. Mackie, J. McNaughton, J. Miles, S. Neill, M. Piggott, D. Risch, B. Scott, C. Sparling, T. Stallard, P. Thies, S. Walker, D. White, R. H. J. Willden, and B. Williamson, "A review of the uk and british channel islands practical tidal stream energy resource," Proceedings of the Royal Society A, vol. 477, no. 2255, p. 20210469, 2021.

[2] W. Batten, A. Bahaj, A. Molland, J. Chaplin et al., "Experimentally validated numerical method for the hydrodynamic design of horizontal axis tidal turbines," Ocean engineering, vol. 34, no. 7, pp. 1013–1020, 2007.

[3] S. W. Tucker Harvey, X. Chen, D. T. Rowe, J. McNaughton, C. R. Vogel, T. Bhavsar, K. amd Allsop, J. Gilbert, T. Mullings, H. Stallard, I. Benson, A. Young, and R. Willden, "Tidal turbine benchmarking project: Stage i - steady flow experiments," in The 15th European Wave and Tidal Energy Conference, 2023.

[4] R. H. J. Willden, X. Chen, S. W. Tucker Harvey, H. Edwards, C. R. Vogel, K. Bhavsar, T. Allsop, J. Gilbert, P. Schmitt, H. Mullings, D. Apsley, T. Stallard, F. Zilic de Arcos, M. A. Dufour, C. Choma Bex, G. Pinon, A. I. Evans, I. Masters, L. H. da Silva Ignacio, C. A. R. Duarte, F. J. Souza, S. Gambuzza, Y. Liu, I. M. Viola, M. Rentschler, T. Gomes, G. Vaz, R. Azcueta, H. Ward, F. Salvatore, Z. Sarichloo, D. Calcagni, T. T. Tran, H. Ross, M. Oliveira, R. Puraca, and C. B. S, "Tidal turbine benchmarking project: Stage i - steady flow blind predictions," in The 15th European Wave and Tidal Energy Conference, 2023.

[5] G. T. Scarlett, B. Sellar, T. van den Bremer, and I. M. Viola, "Unsteady hydrodynamics of a full-scale tidal turbine operating in large wave conditions," Renewable Energy, vol. 143, pp. 199–213, 2019.

[6] G. T. Scarlett and I. M. Viola, "Unsteady hydrodynamics of tidal turbine blades," Renewable Energy, vol. 146, pp. 843–855, 2020.

[7] G. T. Scarlett, B. Sellar, T. van den Bremer, and I. M. Viola, "Unsteady hydrodynamics of a full-scale tidal turbine," in The 6th European Conference on Computational Mechanics, 2018.

[8] G. T. Scarlett and I. M. Viola, "Hydrodynamics of tidal turbine blades," in The 13th European Wave and Tidal Energy Conference, 2019.

[9] G. Pisetta, R. Le Mestre, and I. M. Viola, "Morphing blades for tidal turbines: A theoretical study," Renewable Energy, vol. 183, pp. 802–819, 2022.

[10] S. Gambuzza, S. Ōtomo, Y. Liu, A. M. Young, R. Broglia, M. Felli, E. D. McCarthy, and I. M. Viola, "Design and demonstration of a passive pitch system for tidal turbines," in The 15th European Wave and Tidal Energy Conference, 2023.

[11] M. Drela, "Xfoil: An analysis and design system for low reynolds number airfoils," in Low Reynolds Number Aerodynamics: Proceedings of the Conference Notre Dame, Indiana, USA, 5–7 June 1989. Springer, 1989, pp. 1–12.

[12] J. Van Ingen, "The en method for transition prediction. historical review of work at tu delft," in 38th Fluid Dynamics Conference and Exhibit, 2008, p. 3830.

[13] P. J. Roache, Verification and validation in computational science and engineering. Hermosa Albuquerque, NM, 1998, vol. 895.

[14] I. M. Viola, P. Bot, and M. Riotte, "On the uncertainty of cfd in sail aerodynamics," International journal for numerical methods in fluids, vol. 72, no. 11, pp. 1146–1164, 2013.

[15] C. Cummins, M. Seale, A. Macente, D. Certini, E. Mastropaolo, I. M. Viola, and N. Nakayama, "A separated vortex ring underlies the flight of the dandelion," Nature, vol. 562, no. 7727, pp. 414–418, 2018.

[16] C. Cummins, I. M. Viola, E. Mastropaolo, and N. Nakayama, "The effect of permeability on the flow past permeable disks at low reynolds numbers," Physics of Fluids, vol. 29, no. 9, p. 097103, 2017.

[17] E. Wang, K. Ramesh, S. Killen, and I. M. Viola, "On the nonlinear dynamics of self-sustained limit-cycle oscillations in a flapping-foil energy harvester," Journal of Fluids and Structures, vol. 83, pp. 339–357, 2018.

[18] W. Dai, R. Broglia, and I. M. Viola, "Mitigation of rotor thrust fluctuations through passive pitch," Journal of Fluids and Structures, vol. 112, p. 103599, 2022.

[19] B. Chen, S. Su, I. M. Viola, and C. A. Greated, "Numerical investigation of vertical-axis tidal turbines with sinusoidal pitching blades," Ocean Engineering, vol. 155, pp. 75–87, 2018.

[20] I. M. Viola, Z. Gao, and J. Smith, "Use of streamnormal forces within an array of tidal power harvesters," Plos one, vol. 17, no. 7, p. e0270578, 2022.

[21] N. Speranza, B. Kidd, M. P. Schultz, and I. M. Viola, "Modelling of hull roughness," Ocean Engineering, vol. 174, pp. 31–42, 2019.